Fracturing controlled primary migration of hydrocarbon fluids during heating of organic-rich shales

Maya Kobchenko, Hamed Panahi, Francois Renard, Dag Kristian Dysthe, Anders Malthe-Sorenssen, Adriano Mazzini, Julien Scheibert, Bjorn Jamtveit, Paul Meakin

1 **Fracturing controlled primary migration of hydrocarbon fluids during**

2 **heating of organic-rich shales**

3

4 *Maya Kobchenko[1], Hamed Panahi[1,2], François Renard[1,3], Dag K. Dysthe[1], Anders Malthe-*

5 *Sørenssen[1], Adriano Mazzini[1], Julien Scheibert[1], Bjørn Jamtveit[1] and Paul Meakin[1,4,5]*

6

7 [1] Physics of Geological Processes, University of Oslo, Norway

8 [2] Statoil ASA, Oslo, Norway

9 [3] Institut des Sciences de la Terre, Université Joseph Fourier and CNRS, Grenoble, France

10 [4] Idaho National Laboratory, Idaho Falls, USA

11 [5] Institute for Energy Technology, Kjeller, Norway

12

13   **Abstract**

14   Time-resolved three-dimensional *in situ* high resolution synchrotron x-ray tomographic

15   imaging was used to investigate the effects of slowly heating organic-rich Green River Shale

16   from 60° to 400°C, in air without confinement, to better understand primary migration of

17   hydrocarbon fluids in very low permeability source rock. Cracks nucleate in the interior of the

18   sample at a temperature around 350°C. As the temperature increases, they grow and coalesce

19   along lamination planes to form bigger cracks. This process is accompanied by a release of light

20   hydrocarbons generated by decomposition of the initially immature organic matter, as

21   determined by thermogravimetry and gas chromatography. These results provide the first 4D

22   monitoring of an invasion percolation-like fracturing process in organic-rich shales. This process

23   increases the permeability of the sample and provides pathways for fluid expulsion - an effect

24   that might also be relevant for primary migration under natural conditions. We propose a 2D

25   fracture model that reproduces both the observed non-linear crack growth in a lamination plane

26   and the irregular geometry of the crack fronts.

27

1. Introduction

A wide variety of geological phenomena involve the generation and migration of fluids in low permeability rocks. For example, dehydration of sediments in subduction zones generates large fluxes of water that rise along low-permeability subduction interfaces, and provide a mechanism for creep and/or slow earthquakes [*Obara*, 2002]. Similarly, the illitization of clays at depth and the production of methane in organic-rich shales are responsible for the development of overpressure and the formation of piercement structures that are manifest on the surface as mud volcanoes [*Mazzini et al,* 2009]. The emplacement of magmatic bodies into sedimentary basins may also rapidly decompose organic matter, and the resulting gasses may migrate through low permeability rocks in quantities sufficient to bring about mass extinction due to global warming and ozone depletion [*Svensen et al.,* 2004].

Primary migration, *i.e.* the transport of hydrocarbon fluids from extremely low permeability source rocks in which they are generated to more permeable rocks through which they migrate to a trap (reservoir) or to the surface is an example of both economic and fundamental interest. As the organic-rich fine grained sediment from which the source rock is formed is buried, the organic material is transformed into complex high molecular weight/cross-linked organic oil and gas precursors (kerogen). On continued burial, the temperature and pressure rise, and kerogen decomposes into low molecular weight hydrocarbon fluids (gas and oil) which have a much lower viscosity than the kerogen. Part of the generated hydrocarbon fluids escape from the shale into secondary migration pathways, by processes that remain enigmatic, in spite of decades of investigation [*Bjorlykke, 2010*]. The rest is retained in the source rock explaining why shales are becoming an important source of unconventional hydrocarbon fuels, particularly natural gas [*Mohr*, 2010].

51   Fracturing is commonly cited as the most likely mechanism to increase the permeability

52   of source rocks and provide pathways for the generated hydrocarbons [*Vernik*, 1994; *Berg and*

53   *Gangi*, 1999; *Lash and Engelder*, 2005]. During kerogen decomposition, generation of less dense

54   fluids leads to pore-pressure build-up, which may cause cracking of the host rock. The presence

55   of microcracks in shales was highlighted by several authors [*Capuano*, 1993; *Marquez and*

56   *Mountjoy*, 1996], based on 2D imaging techniques. Here we present the first *in situ* 3D

57   experimental investigation of crack formation in organic-rich shale during kerogen

58   decomposition. We show that the 3D crack fronts have complex irregular geometries, and that

59   the fracture process is similar to invasion percolation.

60   Under natural conditions, this fracture process takes place at depths of several kilometers

61   over millions of years, making its monitoring impossible. Therefore, it is very important to

62   construct adequate models of primary migration. Recently, *Jin et al.* [2010] introduced a fracture

63   mechanics model of subcritical crack propagation and coalescence, based on the assumption of

64   linear elastic behavior of the rock. Although the model provides an estimate of the fracture

65   propagation time, the geometry and mechanism of fracture formation were oversimplified. Here

66   we propose a 2D fracture model, assuming short-ranged interactions only, which reproduces the

67   complex crack front shape and the invasion-percolation-like fracturing process observed

68   experimentally.

69   **2. Characterization of Green River Shale samples**

70   The samples were obtained from an outcrop of the organic-rich R-8 unit, of potential

71   commercial interest, in the Green River Formation of the Piceance Basin in northwestern

72   Colorado, USA. It was formed from Eocene lacustrine sediments [*Ruble et al.,* 2001], it presents

73   well-developed lamination and anisotropic mechanical properties [*Vernik and Landis*, 1996] and

74 it contains organic matter (total organic content 9.92 wt%) present in the form of patches of

75 kerogen, distributed preferentially along lamination planes. Before the experiment, this shale had

76 not been exposed to temperatures that would cause significant thermal maturation.

77   Cylindrical core samples (5mm height, 5mm in diameter) cut perpendicular to lamination

78 were prepared for X-ray tomography. Thin sections were taken before and after heating. Thin

79 section microscopy (optical, scanning electron microscopy [SEM]) was performed to map micro-

80 structural features. Optical microscope images highlight the micro-fabric of the shale consisting

81 of alternating light colored carbonate and pyrites-rich lamina with darker clay-rich intervals.

82 Organic-matter can be observed as dark lenses, which are laterally extensive or localized within

83 the clayey and micrite-rich layers (Figure 1A-B). SEM on carbon-coated thin sections using

84 back-scattered electron imagery [BSE] with X-ray spectroscopy was used to identify the

85 elemental composition of the minerals in the matrix. The rock matrix consists of detrital mineral

86 grains with diameters ranging between 10-50 µm, with clay-rich micritic calcite filling the pores

87 in the groundmass. The largest mineral grains are recognized as quartz, pyrites, carbonates and

88 feldspar crystals (Figure 1D).

89   Thermogravimetry [TGA] coupled with gas chromatography-mass spectrometry [GC-

90 MS] was used to analyze the outgoing products during heating, and to determine the temperature

91 of catagenesis. Using TGA, we monitored mass loss of the sample during heating at 10°C/min in

92 air or nitrogen. GC-MS gave information about the amount of outgoing hydrocarbons, water and

93 carbon dioxide during heating at 5°C/min in air or nitrogen. Water release was almost constant

94 between 200 and 1000°C. Carbon dioxide and hydrocarbon emission and mass loss in the

95 thermogravimetry diagram started at around 350°C.

96 **3. Time-lapse 3D imaging and data processing**

97   X-ray tomographic 3D imaging of the shale samples was carried out using beamline ID19

98   at the European Synchrotron Radiation Facility (ESRF) in Grenoble, France. This non-invasive

99   imaging technique measures the absorption of X-rays, to produce a 3D map of X-ray attenuation.

100   The experimental equipment includes a sample manipulator for alignment, a rotation stage for

101   the tomography scan and a high resolution imaging X-ray detector. The 3D data were obtained at

102   a voxel resolution of $5\mu m^3$ at a beam energy of 20 keV.

103   The prepared cylinder was located in a home-built furnace in contact with air, with no

104   confining pressure, and it was gradually heated *in-situ* from 60°C to 400°C at approximately

105   1°C/min. 28 time-lapse scans of this sample were acquired during the heating phase, then several

106   at 400°C. Each scan required 11-14 minutes, and a new scan was started immediately afterwards.

107   Several other samples were imaged before and after heating only, and used to test experimental

108   reproducibility. For all scans, 1500 radiographs were acquired while the sample was rotated over

109   180°. Based on the sets of radiographs, a filtered back-projection reconstructing algorithm was

110   used to calculate the 3D raw-tomograms representing the microporous structure of the sample at

111   different stages of heating. The final 3D volumes were represented by raw files of 830^3 voxels

112   coded in 8-bit gray levels.

113   The 3D images were processed in two ways. First, the strain field both along and

114   perpendicular to lamination were measured, in a typical 2D centered vertical slice of the volume,

115   using digital image correlation [*Hild and Roux*, 2006]. Second, in order to determine crack

116   geometries and track crack propagation, the shape, volume and morphology of the cracks was

117   analyzed in 3D using an imaging software package (AvizoFire ©). Quantitative analysis of the

118   crack formation required isolation of the cracks from the rock matrix. Due to the small crack

119   opening (3-4 voxels), the following procedure was applied: first a binary mask was used to delete

120   the background and the central noisy part of the volumes (imaging artifact); then, an edge-

121   preserving smoothing filter based on Gaussian smoothing combined with a non-linear diffusion

122   algorithm was applied; and finally a "watershed" procedure enabled individual cracks to be

123   isolated [*Sonka et al*, 1999]. The final result of the segmentation process is a series of cracks

124   represented by connected voxels, marked by different labels (represented in different colors in

125   Figure 2A).

126   **4. Observation of deformation and crack formation**

127   A set of thin sections and the tomography images were studied in order to compare

128   petrographic and morphological characteristics of the shale before and after heating. Before

129   heating, organic precursors, which are preferentially oriented parallel to the lamination can be

130   distinguished throughout the sample in the thin section optical images (Figure 1A-B). The color

131   of the shale matrix in the optical images of thin sections after heating was lighter than that before

132   heating due to the loss of organics. Also an abundance of cracks, partially filled with residual

133   organic material, was distributed parallel to the lamination.

134   Tomographic scans of unheated samples identified the densest grains (pyrites) of the

135   shale matrix, which appear as bright inclusions (Figure 1C). The presence of these grains enabled

136   deformation of the sample to be monitored and strain variations to be measured during heating.

137   The analysis of the time lapse 3D imaging during heating revealed two distinct deformation

138   regimes: first the sample expanded almost homogenously, and then the deformation abruptly

139   localized at open cracks. The 2D correlation analysis showed different strain evolutions with

140   temperature depending on the direction. Strain along lamination increased linearly with

141   temperature from 0 at 60°C to 0.6% at around 350°C (just before cracks appeared). Strain

142   perpendicular to lamination increased almost linearly from 0 at 60°C to 1.2% at 290°C, before

143   increasing rapidly to 1.9% at around 350°C.

144   3D image analysis was then performed to determine the geometry of propagating cracks.

145   Figure 2A shows a 3D rendering of the fracture pattern at T=391°C and Figures 2B and 2C show

146   a cut perpendicular to the lamination. The general direction of crack propagation follows

147   lamination planes (no perpendicular fracture was observed). They have essentially constant

148   aperture widths (typically 15-20 micrometers) and rough surfaces in both the horizontal and

149   vertical planes. Figure 3 shows the time evolution of crack propagation in a given lamination

150   plane. As the temperature rises, cracks nucleate, grow and coalesce in a quasi-static manner until

151   they almost fill the plane. Pyrite grains, which can be seen as bright spots in the tomography

152   images (Figure 2C), affect crack growth by pinning the crack front, and control the out-of-plane

153   excursions of the crack path.

154   **5. Discrete model of crack propagation**

155   Based on the fracturing behavior observed during the experiments, a 2D model of in-

156   plane crack nucleation and growth during shale maturation was developed. The model contains

157   the minimum number of components needed to reproduce the key characteristics of the crack

158   growth process (see Supplementary Material). The model focuses on a layer of shale that

159   fractures more rapidly than nearby layers because it has higher kerogen content and/or it is

160   weaker. The layer is modeled by a regular square lattice in which every site represents a small

161   organic-rich shale element. The temperature rises gradually with time and kerogen decomposes,

162   causing a progressive pressure build-up. Each site is characterized by a breaking threshold $\sigma_{c,i}$,

163   and when the pressure exceeds this threshold $p_i > \sigma_{c,i}$, the site breaks and either nucleates a new

164   crack or increases the size of a pre-existing crack. This relaxes the stress, which is distributed

165   equally to the nearest neighbours (long-range elastic interactions are neglected), bringing them

166   closer to failure. This was implemented by reducing the breaking threshold, $\sigma_{c,i} \rightarrow \sigma_{c,i} - d\sigma$, for

167   all nearest neighbors. Each crack is represented by a cluster of broken sites. As soon as sites

168   belonging to different clusters become adjacent, both clusters are merged to form a single crack,

169   and all the merged sites are given the same label/color.

170   Figure 4A shows three successive snapshots during a simulation. In the early stage, the

171   system contains many small independent cracks. Each crack has a rough front, and over time,

172   individual cracks grow slowly and merge until the whole plane is covered. Figure 4B displays

173   the increase of the surface area of the largest final simulated crack. Crack growth occurs in three

174   stages: (1) the fractures are all separated and their surface areas grow gradually; (2) the fractures

175   start to connect and their areas increases in small jumps; and (3) after some time, the system is

176   dominated by one large fracture, with an area that grows by intermittent increases. This

177   intermittent growth dynamics is similar to the behavior of cellular automata earthquake models

178   [*Bak*, 1987] and the crack pattern grows like those produced by invasion percolation processes

179   [*Dias and Wilkinson*, 1986].

180   We suggest that this local deformation approach to the modeling of crack propagation in

181   tight rocks can be applied to other geological systems in which chemical reactions induce

182   volume increase and stress build-up within the rocks. These systems are widespread, including

183   weathering of rocks near the surface [*Røyne et al*., 2008], dehydration of serpentines in

184   subduction zones [*Jung et al.,* 2004] and primary migration of hydrocarbons.

185   **6. Discussion and conclusion**

186   Fracturing during fluid generation in a tight organic-rich rock (oil shale) was investigated

187   experimentally using thin section imaging (optical and SEM), gas chromatography,

188 thermogravimetry and 3D x-rays tomography. At temperatures below ≈300°C degrees, the

189 sample undergoes a simple linear expansion, with an anisotropy related to the rock lamination.

190 Above 300°C, the expansion perpendicular to lamination significantly accelerates up to a

191 temperature of ≈350°C, the temperature at which the first cracks can be detected on the 3D

192 images. Thermogravimetry analysis indicates rapid mass loss in the same temperature range, and

193 chromatography of the outgoing gas indicates kerogen decomposition.

194   Time-resolved high-resolution synchrotron x-rays tomography allowed us to follow the

195 dynamics of the fracturing process accompanying hydrocarbon expulsion. At 350°C, many small

196 cracks were nucleated. With continued heating and kerogen decomposition, cracks grow parallel

197 to lamination and coalesce, until a percolating crack network spanning a single lamination plane

198 has formed. This process occurs simultaneously on different lamination planes. In our

199 experiments, cracks propagate due to heating. However, we emphasize that the crack

200 propagation mechanism we observed might be of much wider relevance since nucleation, growth

201 and coalescence has been observed in a large variety of heterogeneous rocks under different

202 loading conditions (see e.g. [*Moore and Lockner*, 1995]).

203   The analysis of the evolution of the area of the biggest crack in a given lamination plane

204 (Figure 4C) shows a very slow initial increase followed by a rapid increase as cracks coalesce.

205 We managed to qualitatively reproduce this behavior (Figure 4B) with a 2D model, based on the

206 assumption of nearest-neighbor stress transfer upon cracking. The crack patterns are similar to

207 the irregular crack fronts observed in the experiment and the non-linear crack growth also occurs

208 through the sudden merging of individual cracks.

209   Our results provide the first 4D monitoring of an invasion percolation-like fracturing

210 process in organic-rich shale. Most likely, cracks are caused by local volume increase and stress

211 generation produced by organic matter decomposition. These growing and coalescing cracks

212 enhance the permeability of the sample and the hydrocarbon fluids generated by kerogen

213 decomposition can escape through the dynamically created pathways. Similar mechanisms might

214 be relevant for primary migration under natural conditions.

215 Several questions remain open. What is the origin of the anomalous vertical thermal

216 expansion of the sample between 300 and 350°C, well before any crack can be detected on the

217 images? It might be the signature of the nucleation of microcracks with a size much smaller that

218 the spatial resolution of our 3D imaging, throughout the volume of the sample. What would be

219 the effect of stress and/or confinement similar to that in natural environments? It would probably

220 cause the fractures to close once the fluid has escaped, making it difficult to identify the fracture

221 network in exhumed rock samples.

222

226

227   **References**

228   Bak, P. (1996), How Nature Works: The Science of Self-Organized Criticality, *New York, USA.*

229   Bjørlykke, K. (2010), Petroleum Geoscience: From Sedimentary Environments to Rock Physics,

230   *Springer, Berlin, Germany.*

231   Berg, R.R., and A.F. Gangi (1999), Primary migration by oil-generation microfracturing in low-

232   permeability source rocks: application to the Austin Chalk, Texas, *AAPG Bull., 83, 727-756.*

233   Capuano, R.M. (1993), Evidence of fluid flow in microcracks in geopressured shales, *AAPG*

234   *Bull., 77, 1303-1314.*

235   Dias, M. M., and D. Wilkinson (1986), Percolation with trapping, *J. Phys. A. Math. Gen.,*19,

236   3131.

237   Hild, F., and S. Roux (2006), Digital Image Correlation: from Displacement Measurement to

238   Identification of Elastic Properties – a Review, *Strain, 42, 69-80.*

239   Jin, Z.-H., S. E. Johnson, and Z. Q. Fan (2010), Subcritical propagation and coalescence of oil-

240   filled cracks: Getting the oil out of low-permeability source rocks, *Geophys. Res. Lett., 37,*

241   L01305

242   Jung, H. (2004), Intermediate-depth earthquake faulting by dehydration embrittlement with

243   negative volume change, *Nature, 428, 6982, 545-549.*

244   Lash, G.G., and T. Engelder (1992), An analysis of horizontal microcracking during catagenesis:

245   Example from Catskill delta complex, *AAPG Bull., 89, 1433-1449.*

246   Marquez, X.M., and E.W. Mountjoy (1996), Microcracks due to overpressure caused by thermal

247   cracking in well-sealed Upper Devonian reservoirs, deep Alberta basin, *AAPG Bull., 80, 570-*

248   *588.*

249 Mazzini, A., Svensen, H., Planke, S., Guliyev, I., Akhmanov, G.G., Fallik, T., and Banks, D.,

250 (2009), When mud volcanoes sleep: Insight from seep geochemistry at the Dashgil mud volcano,

251 Azerbaijan, *Marine and Petroleum Geology, 26, 1704-1715.*

252 Mohr, S., and G. Evans (2010), Long term prediction of unconventional oil production, *Energy*

253 *policy, 38, 265-276.*

254 Moore, D. E. and Lockner, D.A. (1995) The role of microcracking in shear-fracture propagation

255 in granite, *J. Struct. Geol., 17, 95-114*

256 Obara, K. (2002), Nonvolcanic deep tremor associated with subduction in southwest Japan,

257 *Science, 296, 1679-1681.*

258 Røyne, A., Jamtveit, B., Mathiesen, J., and Malthe-Sorrenssen A. (2008), Controls of rock

259 weathering rates by reaction-induced hierarchical fracturing, *Earth Planet. Sci. Lett., 275, 364-*

260 *369.*

261 Ruble, T. E., M.D. Lewan, and R.P. Philp (2001), New insights on the Green River petroleum

262 system in the Uinta basin from hydrous pyrolysis experiments, *AAPG Bull., 85, 1333 -1371.*

263 Sonka, M., Hlavac, V., and R. Boyle (1999), Image processing, analysis and machine vision,

264 *PWS Publishing, Pacific Grove, CA, USA.*

265 Svensen, H., Planke, S., Malthe-Sorenssen, A., Jamtveit, B., Myklebust, R., Eidem, T.R., and

266 S.S.Rey (2004), Release of methane from a volcanic basin as a mechanism for initial Eocene

267 global warming, *Nature, 429, 6991, 542-545.*

268 Vernik, L. (1994), Hydrocarbon-generation-induced microcracking of source rocks, *Geoph., 59,*

269 *555-563.*

270 Vernik, L., and C. Landis (1996), Elastic anisotropy of source rocks: Implications for

271 hydrocarbon generation and primary migration, *AAPG Bull., 80, 531-544.*

272 **Figure 1:** Finely laminated Green River Shale samples before heating. (A) Optical image of

273 interlaminated silt and clay minerals. (B) Enlarged optical image of a kerogen patch located

274 between silt grains. (C) X-ray tomography slice of the sample, perpendicular to lamination.

275 Bright spots are pyrites grains. (D) Back scattered electron micrograph of silt layer including

276 cracks filled with organics (arrows) surrounded by feldspar (f), pyrite (p), carbonate (c) and

277 quartz (q) grains.

278 **Figure 2:** Tomography images of the shale sample after heating. (A) 3D rendering of final crack

279 network. Each crack corresponds to a different color. (B) 2D slice showing (dark) elongated

280 cracks parallel to the bedding. The central vertical noisy line is an artifact of the micro-

281 tomography technique. (C) Enlargement of (B) showing a crack around a grain of pyrite (arrow).

282 **Figure 3**:

283 Crack propagation dynamics in a lamination plane. (A) Many small cracks nucleated around

284 350°C. Each crack has a different color. (B) Cracks grow with temperature. (C) At some critical

285 stage all cracks have merged into a single sample-wide crack. The circular central region was

286 removed because of a data acquisition artifact.
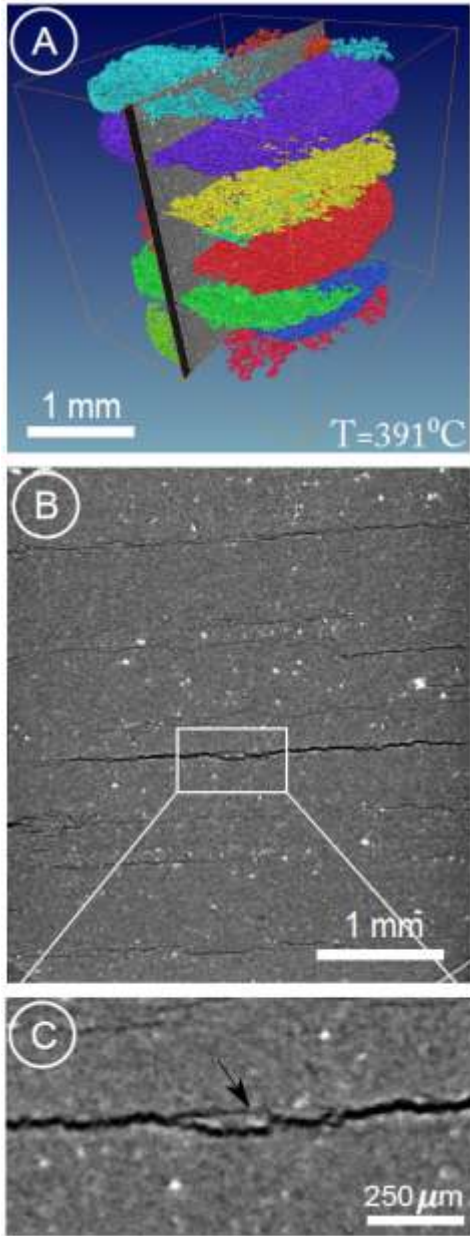
287 **Figure 4:**

288 2D model of primary migration-related fracturing. (A) Three stages of the evolution: nucleation,

289 growth and percolation of cracks. (B) Growth of the area of the biggest crack as a function of

290 time (i.e. kerogen reaction progress). (C) Analogous evolution in a lamination plane in the

291 experiment. The decrease observed after temperature 390°C corresponds to partial crack closing
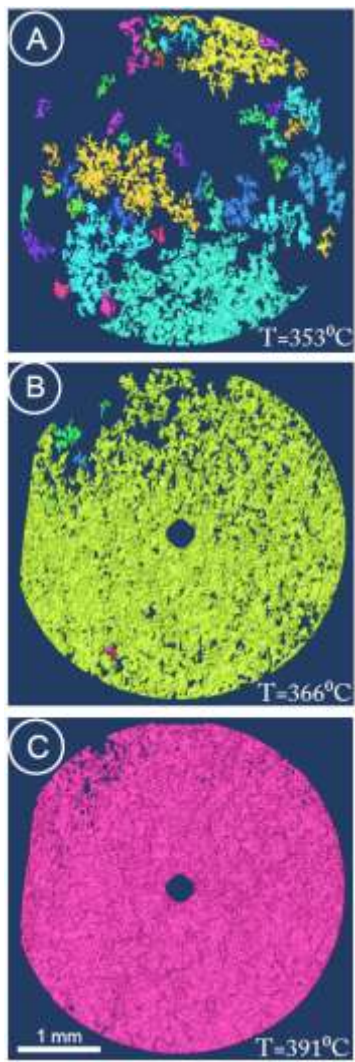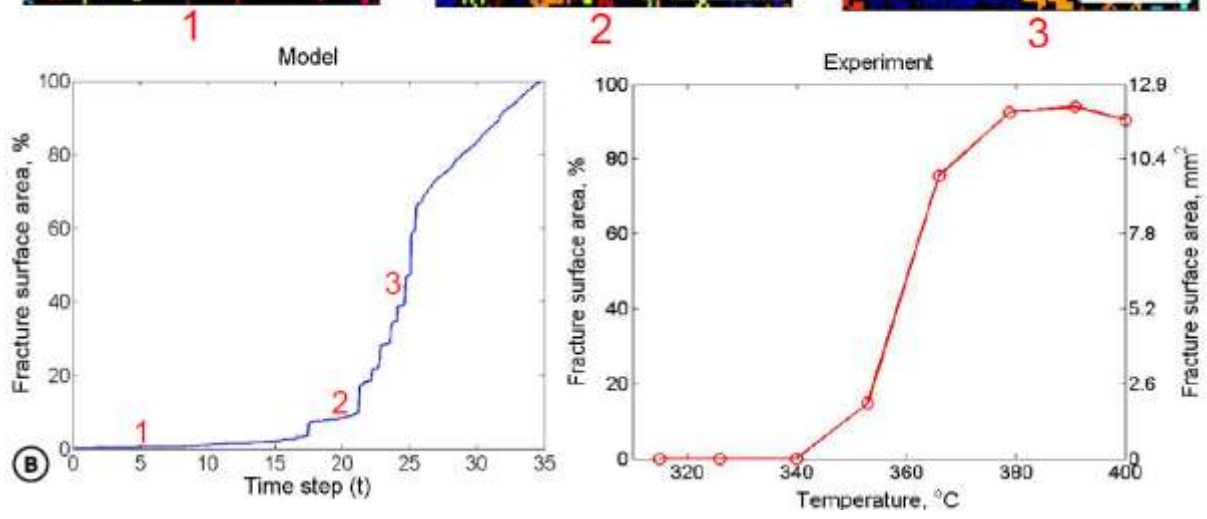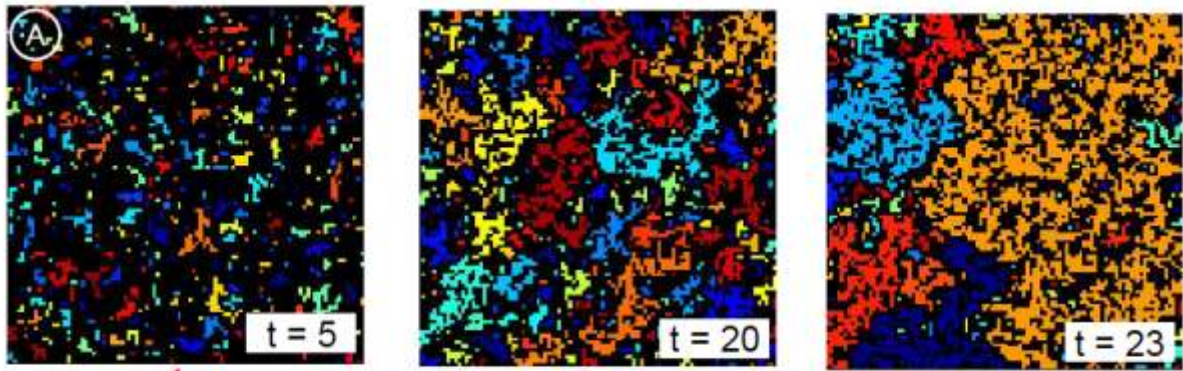
292 after fluid expulsion.

293

Figure 1

16
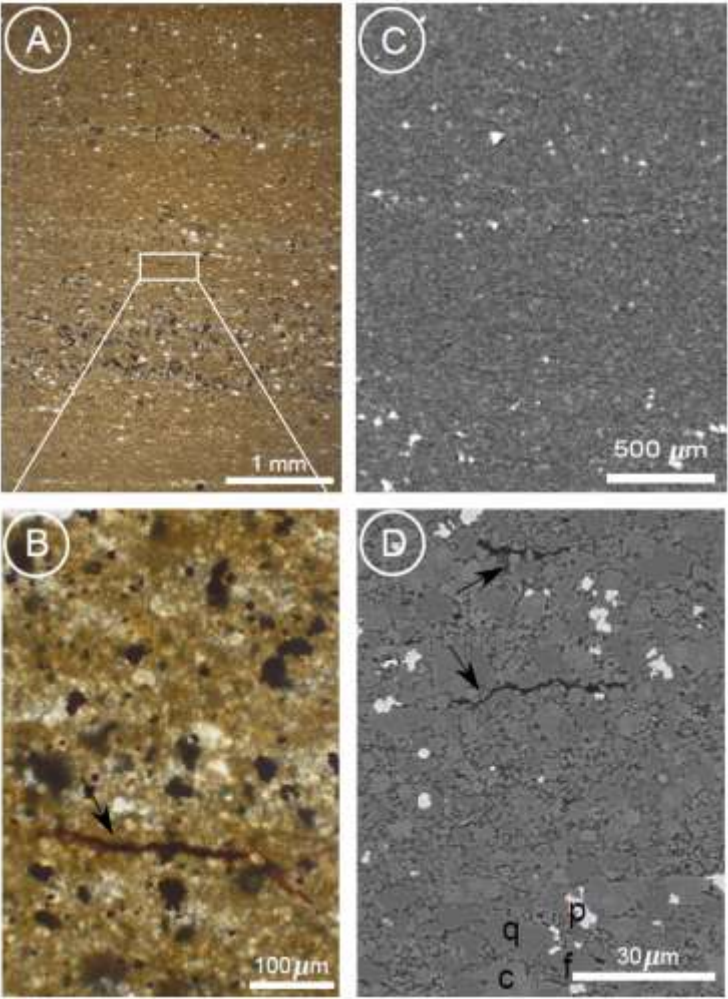
295
296 **Figure 2**

297

298 **Figure 3**

18

299

300 **Figure 4**

301

302